IEEE Access
Multidisciplinary | Rapid Review | Open Access Journal

Received August 4, 2020, accepted August 9, 2020, date of publication August 13, 2020, date of current version August 25, 2020.

Digital Object Identifier 10.1109/ACCESS.2020.3016213

Fault Diagnosis of Power Transmission Lines Using a UAV-Mounted Smart Inspection System

SAN KIM[1], DONGGEUN KIM[1], SIHEON JEONG[1], JI-WAN HAM[1], JAE-KYUNG LEE[2], AND KI-YONG OH[1]

[1]Department of Energy Systems Engineering, Chung-Ang University, Seoul 06974, South Korea
[2]KEPCO Research Institute, Daejeon 34056, South Korea

Corresponding author: Ki-Yong Oh (kiyongoh@cau.ac.kr)

This work was supported in part by the Korea Electric Power Corporation through the KEPCO Research Institute under Grant R16TA26, and in part by the Chung-Ang University Graduate Research Scholarship in 2019.

ABSTRACT Fault diagnosis of power transmission systems (PTSs) is crucial for ensuring the reliability of power grids because most grids are exposed to harsh environments. For integrity diagnosis of PTSs, this article proposes a nondestructive patrol inspection method that employs a smart inspection system (SIS) mounted on an unmanned aerial vehicle (UAV). This system overcomes the geographical limitations faced in accessing PTSs. The SIS includes an ultraviolet camera system that can detect partial discharges on the damaged surfaces of PTSs. The SIS is characterized by three main features. First, it employs an automatic line-tracking method based on image-processing methods. Second, defect locations are automatically estimated on the basis of the consistency of partial discharges, where consistency indicates the steadiness of corona discharges in one-dimensional global coordinates. Third, an alarm is triggered on the basis of the combination of the result from a statistical outlier detection method and the estimated partial discharge locations on a two-dimensional partial discharge map. Finally, a UAV equipped with the proposed system is field-tested for PTS inspection in the autopilot mode. Field tests conducted on ultrahigh-voltage PTSs confirmed the damage detection capabilities of the proposed method and demonstrated its effectiveness and convenience.

INDEX TERMS Fault diagnosis, transmission lines, ultraviolet camera, unmanned aerial vehicle.

I. INTRODUCTION

Power transmission systems (PTSs), which consist of transmission lines (TLs) and auxiliary systems, are the lifeline of modern industries and civilization because electricity is a major energy source for most systems and facilities. Several methods and systems, including coordinated emergency controls, adaptive relaying, intelligent inspection, and flexible AC transmission systems, have been developed to enhance the reliability and safety of power grids and their auxiliary systems, and thereby, minimize the possibility of widespread blackouts [1], [2]. Among them, intelligent inspection of power facilities has attracted considerable attention with the advent of the fourth industrial revolution, which has led to technological advances in mobility and novel sensors. The products of this revolution are particularly useful for proactive and condition-based operation and maintenance of PTSs, which are not only susceptible to various types of failures [3] in harsh environments but are also difficult to inspect owing to their geographical extent and overhanging nature.

In intelligent diagnosis, a power system component of interest is automatically inspected for damages or failures, and the damaged components are repaired or replaced using state-of-the-art technologies. Two technological innovations of the fourth industrial revolution are promising for use in intelligent inspection: Internet of Things (IoT) and mobility [4].

IoT facilitates the real-time collection of all condition-related data about PTSs and the transmission of these data to a cloud server linked to a supervisory control and data acquisition system. The accumulated big data can be used as health or fault indicators if they can be appropriately managed and processed using artificial intelligence. A major concern with this approach is the high initial cost of on-site installation of IoT sensors and artificial-intelligence-embedded cloud servers because of the large expanse of PTSs.

The associate editor coordinating the review of this manuscript and approving it for publication was Amjad Anvari-Moghaddam.

By contrast, mobility solutions based on novel sensors can be used to conduct scheduled maintenance [5], [6]. However, they cannot be used for real-time inspection because the data are collected during relatively short periods of time. Nevertheless, they are more cost-effective than IoT-based operation and maintenance of PTSs. Furthermore, mobility solutions can help overcome the constraints associated with accessing overhead PTSs, which are typically 50–100 m above the ground or higher in the case of ultrahigh-voltage lines [7]. These advantages have spurred utility companies to develop mobile robots equipped with novel inspection systems [6]. In particular, unmanned aerial vehicles (UAVs) are currently in the limelight because they are small, precisely controllable, and cost-effective. However, owing to their limited payload capacity, they can carry only noncontact-type sensors for fault diagnosis. Therefore, UAV-based inspection systems should be designed by considering these limitations [8].

Noncontact-type sensors include infrared thermal imaging cameras, microphone arrays, and ultraviolet (UV) cameras [9], [10]. They are useful for detecting the damaged surfaces of ultrahigh-voltage conductors and auxiliary components, which not only cause partial discharges (PDs)—also termed ''corona discharges''—but also emit UV rays, ultrasound, and thermal energy [11]. However, when a microphone array is mounted on a UAV to detect ultrasound, the sound generated by the UAV blades significantly increases the background noise level, rendering the microphone array insensitive to the ultrasound emitted from PTS faults [12]. Furthermore, UAV-mounted infrared thermal cameras cannot estimate the temperature of PTSs accurately in external environments because many of the parameters used to convert thermal energy into temperature show strong dependence on the surrounding environment [13]. Hence, parameter tuning for an infrared thermal camera depends on the weather and surroundings, which indicates that the recording of thermal images requires significant efforts. Consequently, the use of infrared thermal cameras for detecting PTS defects is generally confined to controlled environments, such as inside buildings and in underground tunnels.

The benefits and drawbacks of mobility- and sensor-based solutions suggest that it would be useful to develop an inspection system composed of a UV camera mounted on a UAV. UV cameras are robust to sound from rotating blades and vibrations during UAV flights, which means that they can sense UV rays from PTSs even in the presence of sound and vibrations [3], [14]. From the mobility perspective, a UAV is a cost-effective solution for electric utilities for the maintenance of transmission facilities, and it eliminates geographical limitations.

In this study, we have developed a smart inspection system (SIS) that can be mounted on a UAV for patrol inspection of TLs and auxiliary systems of PTSs. The proposed SIS employs several novel methods. First, the weight of the SIS is optimized for weight reduction because the system weight determines the inspection time and the system's economic efficiency when the system is mounted on a UAV. Second, because manual gimbal control degrades the inspection performance, an automatic line-tracking method is developed for maintaining a targeted TL at the center of the field of view of the UV camera. This is necessary to realize automatic inspection. Notably, the inclusion of manual gimbal control in the SIS could adversely affect fault diagnosis because there is a high likelihood of the operator being distracted over long inspection periods. If the electrician (or operator) is distracted and fails to operate the SIS to capture UV images of PTSs, the inspection would have to be repeated, leading to time and cost escalations. Third, a method is devised to estimate the steadiness of PD occurrence as an initial indicator for fault detection. This method is expected to be useful for patrol inspection of PTSs, which, thus far, has been conducted by electricians by using portable equipment and naked eyes. Patrol inspection of PTSs at power facilities helps detect potential defects, and a precise inspection involving the recording of UV images over a one-minute interval is subsequently conducted. The occurrence of more than 5000 PDs/min is considered a fault, and a damaged PTS is repaired or replaced [15]. Note that initial patrol inspections require significant effort, particularly in Korea, where most TLs are located in mountainous regions, which cover more than 70% of the Korean territory. Fourth, for alarm generation, a statistical outlier detection method is developed in combination with a method for determining the locations of PDs on a two-dimensional (2D) consistency map. Finally, the effectiveness of the proposed SIS mounted on a UAV is confirmed by conducting a field test involving an autopilot flight [16]. Moreover, several interesting phenomena observed in the field test are recorded, and knowledge of these phenomena could be useful for UV-camera-based fault diagnosis in different applications. This study aims to not only alleviate limitations to access PTSs but also improves convenience and efficiency of patrol inspection.

II. HARDWARE CONFIGURATION

The proposed SIS was mounted on a UAV, as shown in Fig. 1. The entire platform was designed to weigh less than 5.5 kg because the maximum payload of the UAV used herein (DJI M600 Pro, CHN) is 5.5 kg, excluding the weight of the UAV itself. Note that for the given power capability, the UAV flight time (i.e., inspection time) decreases significantly for a heavier payload, and therefore, weight reduction should be a major consideration when designing the SIS that is to be mounted on a UAV. For example, the UAV used in this study cannot fly for more than 20–25 min with the maximum payload, which is insufficient for patrol inspection. Evidently, the economic feasibility and inspection efficiency of the operation depend on the weight of the UAV-mounted inspection system.

The hardware components of the proposed SIS are listed in Table 1. A UV camera (OFIL ROMpact, Israel) was positioned on a custom-designed gimbal printed with polylactic acid by using a three-dimensional printer

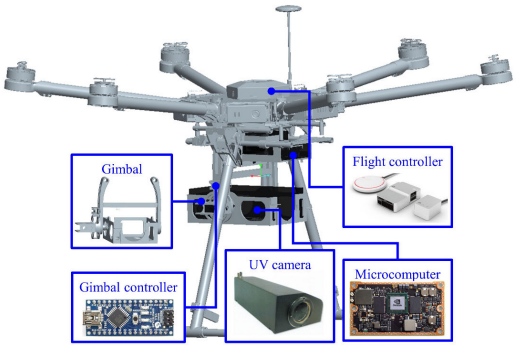

FIGURE 1. Hardware configuration of the SIS mounted on a UAV.

TABLE 1. Hardware components of the SIS mounted on a UAV.

Part	Name	Weight	Remark
UAV	M600 Pro	5.5 kg (UAV + FC)	-
Flight controller	A3		
UV camera	ROMpact	1.5 kg	FOV: 8° × 6°
Gimbal	-	0.73 kg	PLA
Gimbal controller	Arduino Nano	7 g	-
Servomotor	HS-7950TH	68 g	35 kg·cm
Microcomputer	Jetson TX2	0.2 kg	-

(Ultimaker S5, Netherlands). The UV camera records UV images with a UV sensor and visible images with an optical sensor and provides a combined image. According to the manufacturer, the camera has a guaranteed measurement range of up to 50 m for corona discharges, and the measurement range depends on the intensity of the corona discharge being recorded. The horizontal and vertical angles of view of the UV camera were 8° and 6°, respectively, which correspond to the horizontal and vertical spans of 3.50 and 2.62 m, respectively, for an inspection object located 25 m away. This distance (25 m) is safe for avoiding global positioning system (GPS) signal distortion and magnetic interference between the onboard geomagnetic sensor and the energized AC power conductors [16].

The fabricated gimbal was used to control the tilt angle of the UV camera. We equipped the gimbal with a servomotor (Hitec HS-7950TH, Republic of Korea) that provides 35 kg·cm of torque at 7.4 V and has a deadband of 2 μs, as well as with a tilt-angle controller (Arduino Nano). A microcomputer (NVIDIA Jetson TX2, USA) with a dual-core Denver 2 64-bit central processing unit and a quad-core ARM A57 complex was mounted on the custom-designed gimbal to calculate the tilt angle for automatic line-tracking and to record inspection images from the UV camera and GPS information from the flight controller (DJI A3, CHN) embedded on the UAV.

The weight of the UV camera was 1.50 kg and that of the custom-designed gimbal was only 0.73 kg because of the low density of the material (1.24 g/cm^3) used to print it. By contrast, commercially available gimbals for UAVs generally weigh more than 2 kg. The auxiliary components of the SIS, such as the minicomputer, gimbal controller, cables, and connectors, weighed 1.02 kg in total. The total weight

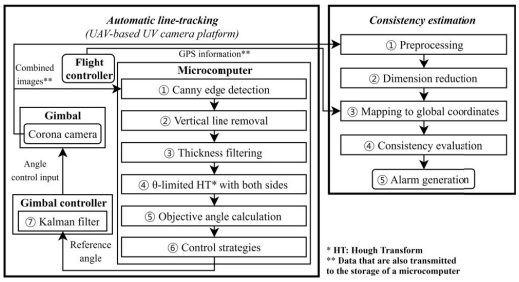

FIGURE 2. Overall fault diagnosis algorithm.

of the SIS, which comprised the custom-designed gimbal, UV camera, and auxiliary SIS components, was 3.25 kg, resulting in a flight time of 35 min, which is sufficient for patrol inspections. Specifically, this flight time of the UAV with the SIS guarantees the inspection of six phase conductors in one span because three phase conductors are generally hung on each side of PTSs. Hardware optimization is not described in detail in this article because it is beyond the scope of this study.

III. FAULT DIAGNOSIS METHOD

The fault-diagnosis principle employed in the proposed method is as follows: PDs that constantly emit from the damaged surfaces of power systems can be detected using a UV camera because their wavelengths are in the UV range [10]. Furthermore, the PDs recorded using a UV camera in the moving coordinate system of the UAV can be transformed to steady occurrences at a certain location, namely, the damaged surface, in the global coordinate system. Steady occurrence of PDs is termed consistency hereinafter. In other words, consistency is the invariability of PD locations. PDs on damaged surfaces exhibit consistency unlike randomly occurring noises. Therefore, a PD with consistency can imply a defect in the power system. This principle suggests that the consistency of PDs in the global coordinate system is an effective health indicator for fault diagnosis in patrol inspections, where all PTS segments are measured for less than 5 s.

Fig. 2 shows a flowchart of the proposed fault diagnosis algorithm. The algorithm consists of two main parts: automatic line-tracking (part *A*) and consistency estimation (part *B*). In part *A*, combined 2D inspection images, in which the visualized PDs are overlaid on visible-spectrum images, are collected. A method for autonomously tracking TLs is applied to ensure that the target TL is always located at the vertical center of the recorded images. In part *B*, several images and signal-processing methods are employed to effectively identify the consistency of PDs and generate alarms. Alarm generation compares the frequency and locations of these PDs.

A. AUTOMATIC LINE-TRACKING

In part A, for efficient patrol inspection, the inspection images of PTSs are recorded by the SIS by using the proposed automatic line-tracking method. As shown in Fig. 2, combined images from the UV camera system and GPS information from the flight controller are transmitted to

the microcomputer. The locations of PTSs are identified from the transmitted combined images and, subsequently, a reference gimbal angle is calculated and transmitted to the gimbal controller that controls the tilt angle of the gimbal on which the UV camera is mounted.

The proposed automatic line-tracking method helps maintain a targeted TL at the vertical center of the recorded image based on two major characteristics of TLs. First, in the global coordinate system, the slope of a TL is closer to that of a horizontal line than to that of a vertical line, suggesting that horizontal-like lines in the images are candidates for TLs. Second, TLs must pass both the left and right sides of inspection images during inspection, except at the start and end of patrol inspections; this suggests that line tracking is possible by using this characteristic when a targeted TL is labeled at the start of a patrol inspection. To achieve automatic line-tracking based on these two characteristics, the proposed method comprises seven phases (*A* in Fig. 2). The first six phases are executed in the microcomputer, and the last phase is executed in the gimbal controller.

In the first phase, a 2D binary edge map is created by using the three-step Canny edge detection method [17]. In this method, first, a Gaussian filter and nonmaximum suppression are applied to an input image for edge sharpening. In the second step, double thresholds are used to distinguish between weak and strong edges. In the third and final step, a binary edge map is obtained by suppressing the weak edges that are not connected to strong edges.

In the second phase, the vertical lines in the 2D edge map are removed through convolution by using the vertical filter kernel as follows:

$$[1 \quad 2 \quad 3]^{\mathrm{T}}. \tag{1}$$

Pixels with a convolution result that differs from 2 are suppressed. This procedure removes vertical consecutive edges and retains only horizontal edges. The vertical filter kernel is used to effectively distinguish horizontal edges from vertical edges. This vertical filter kernel is used because only three vertically arrayed pixels in an edge map with the values $[0\ 1\ 0]^{\mathrm{T}}$ yield a convolution result of 2, implying that these pixels do not contain vertical edges. Note that TLs are generally expressed as pairs of nearly horizontal parallel lines on binary edge maps. The pairs of nearly horizontal parallel lines yields a convolution result of 2 when the proposed vertical filter kernel is used. In this phase (i.e., the second phase), several edges with large slopes are excluded to increase the Hough transform [18] accuracy in the fourth phase.

In the third phase, the TLs on the 2D edge map are strengthened through convolution by applying the thickness filter kernel

$$[0.33 \ \ 0.33 \ \ 0.33 \ \ -0.5 \ \ -0.5 \ \ -0.5 \ \ 0.67 \ \ 0.67 \ \ 0.67]^{\mathrm{T}}. \tag{2}$$

Pixels with a convolution result that differs from 1 are suppressed. This thickness filter kernel is used because convolution with it retains only the regions with two edges at an interval of 3–7 pixels, which means that 3–7-pixel-thick TLs in the input image yield a convolution result of 1. Note that the thickness of the TLs in the inspection images depends on the specifications of the UV camera and the distance between the camera and the TLs during an inspection. This suggests that the thickness of the filter kernel should be defined after considering the measurement scheme used for patrol inspection.

In the fourth phase, an image processed for TL extraction in the third phase is subjected to Hough transform [19] by using a first-order polynomial line (i.e., $y = ax + b$) as the reference model. This approach is reasonable because TLs appear as straight lines in inspection images owing to the narrow field of view of the UV camera, despite the TLs conforming to the general catenary curve equation [20]. Specifically, the horizontal length in a recorded image is approximately 3.5 m for an 8° horizontal angle of view when the UV camera is 25 m away from the TLs. The extracted lines include many horizontal-like lines from the surrounding environment. Hence, the angle θ that represents the slope of the lines is limited to the range $-15°$ to $15°$ with respect to a reference line that is defined by the altitudes of two neighboring transmission towers, where it is assumed that the vertical axis of the recorded images represents altitude. Notably, the value of θ depends on the environment near the inspection site. Specifically, the TLs between two towers with a large altitude difference require a larger range of θ values. The θ value range must be set by considering the altitude difference between two towers ($\theta_{\text{altitude difference}}$) as follows:

$$\theta_{\text{altitude difference}} = \arctan\left(\frac{Z_2 - Z_1}{S}\right), \tag{3}$$

where the altitudes of two transmission towers are Z_1 and Z_2, and the span length the two towers is S. Moreover, the aforementioned second characteristic of TLs suggests that only partial regions that include both the left and right sides of a binary edge map should be used instead of the entire binary edge map to reduce the computational burden. In this study, 100 pixels from both the left and right sides were subjected to Hough transform, instead of the entire binary edge map, which had a width of 640 pixels. This reduced the calculation time for Hough transform without reducing accuracy.

In the fifth phase, the target gimbal angle required by the UV camera for orienting the TLs along the vertical center of the inspection image is calculated from the straight lines detected in the fourth phase. The target gimbal angle is defined as the vertical angular distance between the vertical center of the inspection image and the mean vertical center of the lines:

$$z = \left[\sum_{i=1}^{L}\left(\frac{m_i}{L}\right) - C_I\right] \times \frac{\beta}{V}, \tag{4}$$

where z, m_i, and L denote the target gimbal angle (in degrees), vertical distance between the center of an input image and the vertical center of the ith detected line (pixels), and number of lines detected, respectively. C_I, β, and V denote the distance between the bottom and the center of the input image (in pixels), vertical angle of view of the UV camera, and

vertical size of the input image (in pixels), respectively. Note that β/V is the vertical angular distance per pixel of the input image.

In the sixth phase, two control strategies are employed to prevent the UV camera from losing a tracked TL because of significant interference, such as that from adjacent lines that are not currently being inspected. The UV camera may often follow such adjacent lines instead of the targeted TL around waypoints or lose the targeted TL during autopilot flights because the start-stop motion of the UAV at waypoints causes the SIS to vibrate significantly, leading to camera shake. Fluctuations in the inspection image can be grouped into two categories: small disturbances, where the standard deviation of m_i is large and the disturbances cause minor variations in m_i, and large disturbances, which change the mean of m_i significantly. These control strategies have been developed with the aim of maintaining a fixed gimbal angle for tracking the target TL when the deviation of m_i increases or its mean changes significantly because changes in the UAV's position resulting from these disturbances are temporary and the UAV stabilizes quickly ($\approx$0.8 s). Specifically, changes in the target gimbal angle z with respect to the current gimbal angle are set to zero in two cases. In the first case, the standard deviation of m_i exceeds 35% of the vertical size of the input image in pixels. In the second case, the mean of m_i is changed by more than 40% of the input image's vertical size compared to that of a previous input image. The thresholds for these two cases are selected based on the results of preliminary laboratory tests and field measurements.

In the seventh phase, variations in the target gimbal angle due to disturbances associated with aerodynamic loads, such as gusts acting on the UAV, are adaptively filtered by using a Kalman filter [21] to enhance the robustness of tilt control. The optimal parameters of the Kalman filter are set by considering the flight speed, UAV specifications, autopilot flight path, and environmental factors of the inspection site, such as wind speed. Note that the sixth and seventh phases are dual protection measures to avoid losing a tracked TL when the proposed system is used in the field. The field application of the proposed system requires high maturity and integrity to ensure zero accidents.

B. CONSISTENCY ESTIMATION

This section presents a five-phase method for consistency estimation.

In the first phase (B-① in Fig. 2), recorded 2D input images in the red, green, and blue (RGB) format are preprocessed to exclude the background and thereby emphasize the PD measured by the UV sensor.

First, an RGB metric image is converted into the chroma metric form. The chroma metric form is similar to grayscale, but each pixel in the image represents a chroma value [22] calculated from the normalized RGB values as follows:

$$S_{ij} = \begin{cases} \dfrac{V_{ij} - \min(R_{ij}, G_{ij}, B_{ij})}{V_{ij}} & V_{ij} > 0 \\ 0 & V_{ij} = 0, \end{cases} \tag{5}$$

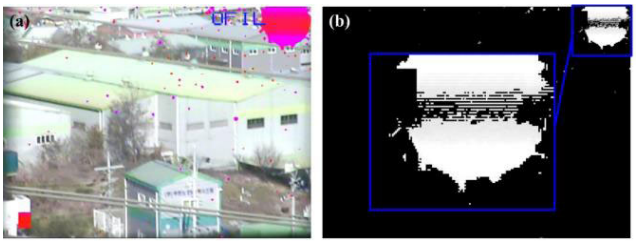

FIGURE 3. Measurement result of the SIS: (a) a combined image, and (b) a chroma metric image with a stripe at the location of a PD and (inset) a cropped corona discharge.

where S_{ij} is the chroma or saturation value (0–1) of the elements in the ith row and jth column of the input image. R_{ij}, G_{ij}, and B_{ij} are the normalized red, green, and blue values of the elements in the ith row and jth column of the RGB metric image form, respectively. These values are defined to lie in the range 0–1. V_{ij} denotes the lightness value (0–1), and it is calculated as

$$V_{ij} = \max(R_{ij}, G_{ij}, B_{ij}). \tag{6}$$

This conversion simplifies the separation of the visualized PDs from the visible-spectrum background, unlike the RGB form, because the color used for visualizing a PD has a higher chroma value than that of most of the background. Note that this preprocessing step can be omitted when UV images are recorded independently from optical images. The UV camera used in this study does not provide two separate images. After image conversion to the chroma metric form, elements in regions with chroma values below 0.9 or with lightness values below 0.6 are set to zero. This procedure eliminates only those background regions that have low or high chroma values with low lightness values. The thresholds for the chroma and lightness values were set by comparing the preliminary laboratory measurements with the field measurements.

Second, the on-screen image displays several unwanted characters such as the name of the UV camera manufacturer. These characters are removed.

Third, the stripes located on the pixels corresponding to PDs are corrected. A stripe is a pattern on a visualized PD, and it is specific to the UV camera employed (Fig. 3(b)). Stripes can occur because the output of the UV camera is transmitted as an analog video signal, which is vulnerable to vibrations. Stripe patterns reduce the accuracy of the proposed method because a few pixels that should be occupied by a PD and that should, therefore, be displayed in white are displayed in black, as shown in Fig. 3(b). In other words, the information in the pixels corresponding to a PD is distorted because of the stripe pattern. Therefore, the stripes are removed by simply adding the value of an adjacent row to every row:

$$I_{ij} = I'_{ij} + I'_{i-1j} \; (i \neq 1). \tag{7}$$

Here, I denotes a preprocessed image in the chroma metric form with M rows and N columns, I_{ij} denotes an element from the ith row and jth column of I after removing the stripes, and I' denotes I before removing the stripes.

In the second phase (B-② in Fig. 2), the preprocessed 2D image I ($M \times N$ matrix form) is reduced to a one-dimensional

(1D) matrix K $(1 \times N)$ with noise suppression by applying the 3σ outlier elimination method [23], [24]:

$$K_j = \begin{cases} \dfrac{K'_j - (\mu + 3\sigma)}{M} & (K'_j - (\mu + 3\sigma) > 0) \\ 0 & else, \end{cases} \quad (8)$$

where K_j represents the PD intensity of each element in K $(1 \times N)$. K' is a 1D matrix in which each element K'_j is the summation of the elements in each column of I, and it is expressed as follows:

$$K' = [\sum_{i=1}^{M} I_{i1} \cdots \sum_{i=1}^{M} I_{ij} \cdots \sum_{i=1}^{M} I_{iN}], \quad (9)$$

where μ is the mean of K'_j, and σ is the standard deviation of the elements K'_j. In this phase, it is assumed that the vertical information in the recorded image can be merged because the PD is recorded using the narrow vertical field of view of the UV camera. The 6° vertical angle of view of the UV camera corresponds to a vertical height of 2.62 m when the inspection object is 25 m away from the camera. The second phase reduces the computational loads of subsequent processes. The 3σ outlier elimination method aims to minimize the effect of noise. It is assumed in this phase that the PD intensity follows a normal distribution, and a PD from a damaged surface is considered an outlier when its intensity is greater than $\mu + 3\sigma$, which corresponds 0.15% of all PDs. Note that 1σ, 2σ, and 3σ correspond to 13.5%, 2.35%, and 0.15% of the abnormal populations in statistics. Thus, suppressing PD intensities under $\mu+3\sigma$ eliminates the PDs that are uniformly distributed over an input image and are considered as white noise under the measurement conditions employed in this study, whereas the PDs concentrated in certain areas, such as those on damaged surfaces, are less affected by the proposed method.

In the third phase (B-③ in Fig. 2), each element of the K $(1 \times N)$ matrices is mapped to the global coordinates to evaluate the distribution of the PD intensity over the inspection range (Fig. 4). First, the range of view R is calculated as follows:

$$R = 2r \times \tan(\alpha/2), \quad (10)$$

where R, r, and α denote the length (in meters) corresponding to the actual horizontal length of the range indicated by the K matrices or an input image; distance between the UAV and the inspection target, which is set and maintained constant during the autopilot flight [16]; and horizontal angle of view of the UV camera, respectively. Second, l_{center}, which is the distance between the inspection start point and the UAV location during corona camera measurement, of each K matrix is evaluated using Vincenty's formula [25]; in this study, the degree of accuracy was set to approximately 6.4 mm, which is equal to one-billionth of the radius of the Earth. Third, the distance l_j between the inspection start point and the location of the jth elements of the K matrices is calculated as follows:

$$l_j = l_{center} - dir(\frac{R}{2} - (j-1)\frac{R}{N-1}), \quad (11)$$

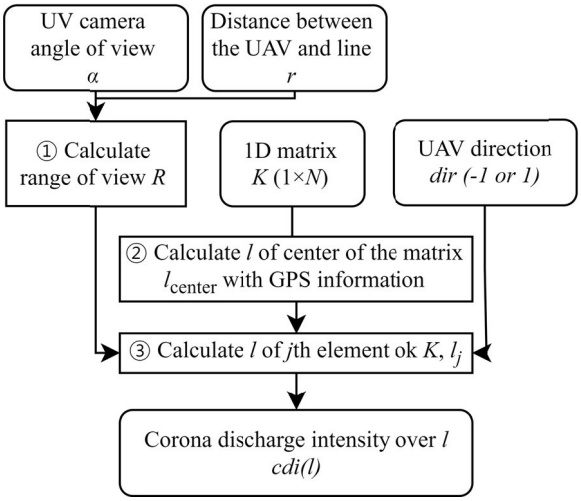

FIGURE 4. Method for mapping the elements of the K matrices to the global coordinate system.

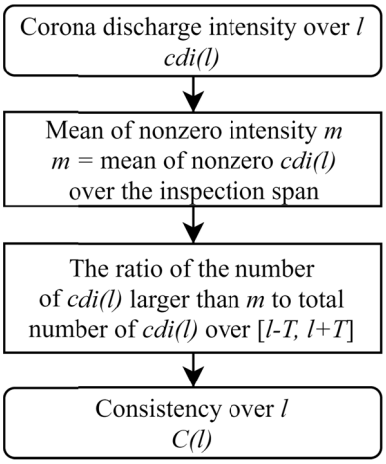

FIGURE 5. Method for mapping in a consistency evaluation.

where *dir* indicates the direction during inspection. On the basis of the direction of motion of the UV camera system relative to the TLs, *dir* is defined as 1 when the UAV moves from the left to the right and as -1 when the UAV moves from the right to the left. Finally, each element in all of the K matrices is arranged using l_j to determine the distribution of PD intensity over the inspection range $cdi(l)$.

In the fourth phase (B-④ in Fig. 2), the consistency of the PD is evaluated, as depicted in Fig. 5. First, only the threshold value of the PD intensity is required to identify intense PDs, such as those emitted from damaged surfaces. This threshold is automatically defined from measurements as the mean of the nonzero PD intensities over the inspection span between two transmission towers m or as the mean of every value in the distribution $cdi(l)$. This is reasonable because the PDs emitted from damaged surfaces in PTSs have a higher intensity than the mean of $cdi(l)$. Finally, the consistency value at l, $C(l)$, is defined as the ratio of the number of PD intensities higher than m to the total number of PD intensities in the interval $[l - T, l + T]$, where T is the tolerance value corresponding to the GPS error and is

set to 1.5 m considering the accuracy of the GPS module used in this study. T can be also described as the size of the moving window in the consistency evaluation. A higher T value implies that a PD at l can appear in a broader range from l, meaning that the distribution of consistency values is flatter. Note that high-intensity noise may be measured during an inspection. However, the occurrence frequency of such noise is not sufficient to affect the magnitude of m. If high-intensity noise occurs frequently, the gain of the UV camera should be lowered during patrol inspections.

The fifth phase (B-⑤ in Fig. 2) generates alarms based on the consistency estimated in the fourth phase. First, a pre-alarm is generated using the 3σ method [24] under the assumption that the consistency values of the PD follow a normal distribution, as aforementioned. Under this assumption, consistent PD emission with high consistency values from damaged surfaces are regarded as statistical outliers in the normal distribution. If a consistency value deviates from the mean by three standard deviations, a pre-alarm is generated. The consistency is then mapped over a relative distance r, where r denotes the relative distance between the UAV and any object perpendicular to the TLs, through consistency estimation for varying r to determine the location of the object that is consistently emitting the PD. In other words, a 2D consistency map is generated. One axis of this map is parallel to the TLs, and the other axis is perpendicular to the TLs. The process of generation of the 2D consistency map coincides with the start of inspection. Based on the results of consistency mapping, a final caution or warning alarm is generated if the location of the maximum consistency value and the target coincide or a consistency value exceeding 80% of the maximum consistency value is observed on the target. A caution alarm is generated if a consistency value deviates from the mean by 3σ, whereas a warning alarm is generated if a consistency value is out by 6σ from the mean. The caution alarm indicates that the PTSs should be carefully monitored, whereas the warning alarm indicates that precise inspections should be conducted, that is, UV images should be recorded for 1 min, and it should be checked whether more than 5000 PDs occur; if so, the corresponding faulty component should be replaced [15] or the expert system should inspect and evaluate the condition of the PTS. Note that an emergency alarm is not included in the proposed method because a PTS is repaired or replaced after precise inspection. The proposed method was not developed for precise inspection but for patrol inspection.

IV. FIELD TESTS AND DISCUSSION

Several field tests were conducted to verify the effectiveness of the SIS and the proposed method. In the field tests, the automatic line-tracking method (A in Fig. 2) was employed by using the SIS mounted on a UAV (Fig. 1). The UAV conducted patrol inspections in the autopilot flight mode, and it was controlled from a ground control station set up by the Korea Electric Power Corporation Research Institute. The safe distance between the UAV and the TLs was set to 25 m for autopilot flights to avoid interference due to magnetic fields [16], and the UAV platform speed was set to 2 m/s. The lower the UAV speed, the more reliable was the patrol inspection. The proposed consistency estimation method (B in Fig. 2) was applied to the recorded inspection images.

TABLE 2. Field test sites.

Site name	TL #	Environment	PD
SB	70-71	Farmland	No
SB	94-95	Factory	Factory
SS	40-41	Combined	Insulator
SS	32-33	Combined	Clouds

Four spans of 345 kV TLs and auxiliary systems in South Korea were inspected. Table 2 summarizes information about these four sites with two transmission towers, where the field tests were conducted on TLs. The Shingimhae-Bukbusan (SB) TLs 70-71 and 94-95 are in Gimhae and Seoseoul-Shingwangmyeong (SS), respectively, and TLs 32-33 and 40-41 are in Gwangmyeong. SB TL 70-71 is surrounded by farmlands, and SB TL 94-95 is surrounded by factories. SS TL 40-41 and 32-33 are surrounded by both farmlands and factories.

A. AUTOMATIC LINE-TRACKING

Fig. 6 shows the image-processing results for the images recorded using the UV camera in each phase and the reference angles calculated for tilt control by using the automatic line-tracking method. Each phase involved the successful completion of the mission. In the first phase (① in Fig. 6), the Gaussian filter shape for Canny edge detection was set to 5×5 pixels and the aperture size to 3 pixels. After the construction of a binary edge map, the vertical edges were removed by the vertical filter kernel (Eq.(1)) in the second phase (② in Fig. 6), and pairs of horizontal edges with specific intervals were emphasized by the thickness filter kernel (Eq.(2)) in the third phase (③ in Fig. 6). Subsequently, the regions with both left and right sides were subjected to the Hough transform in the fourth phase (④ in Fig. 6). Finally, the tilt angle for gimbal control was calculated as the angular distance between the vertical center of the image and the mean vertical center of the detected lines based on Eq. (4) in the fifth phase (⑤ in Fig. 6). This process was executed in real time on the microcomputer to orient a targeted TL along the center of the inspection images during the inspections.

Fig. 7 shows the reference angles calculated during an inspection of the left-top TL in SB TL 94-95. The horizontal axis represents the relative displacement parallel to the TLs from the start of the inspection. The reference angles for the other field tests were similar and are not shown here for the sake of brevity. The reference angles represent the angular distance from center of the UV camera image to the TL being inspected. Hence, a reference angle close to 0 means that the UV camera tracks the objective TL effectively. A reference angle with magnitude greater than 3° indicated that the TLs were out of the field of view of the UV camera in the SIS, which had a 6° vertical angle of view.

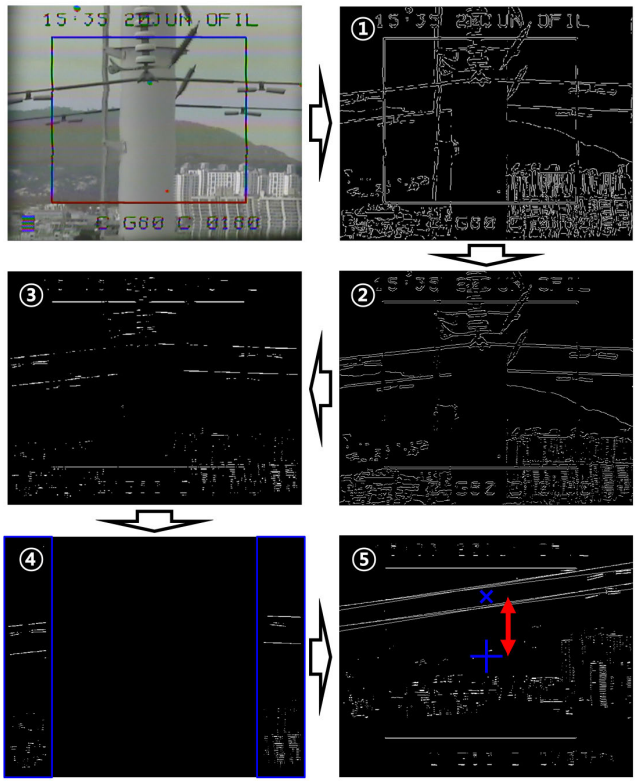

FIGURE 6. Results of the first five phases of the automatic line-tracking method.

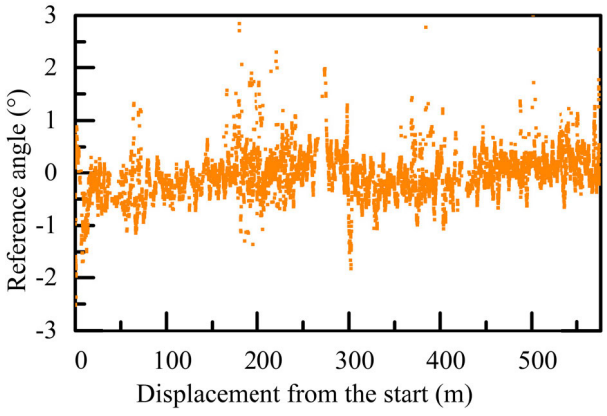

FIGURE 7. Reference angles during inspection of SS TL 40-41 left-top line.

The calculated reference angles were generally within 1° because the UAV flew slowly during inspections. A few large reference angles were calculated around waypoints, and they suggested that smooth flights around waypoints could improve the inspection performance.

The performance of the automatic line-tracking method was evaluated based on the root mean square errors (RMSEs) between the calculated reference angles and the actual gimbal angles during inspections. Specifically, the RMSEs for SS TL 40-41 were 0.45°, 0.43°, and 0.55° for the left-top, left-middle, and left-bottom TLs, respectively, and they corresponded to 36.0, 34.4, and 44.0 pixels in the inspection images with a vertical pixel resolution of 480. It is suggested

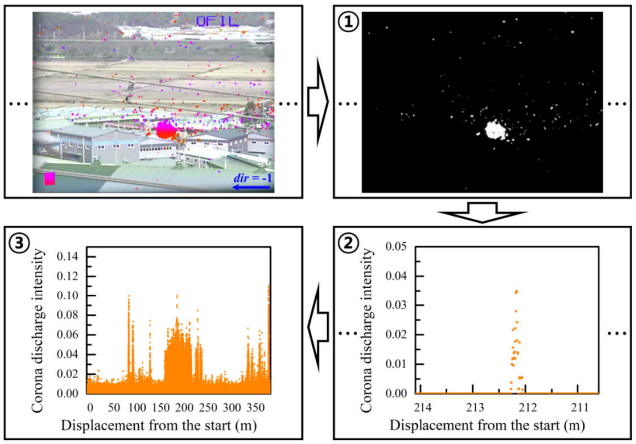

FIGURE 8. Results of the first three phases of the consistency estimation method.

that the TLs were located within 10% from the vertical center, which is equivalent to 48.0 pixels considering the vertical resolution (in pixels) of the recorded image. The largest calculated errors were 3.0°, 2.3°, and 3.1° for the left-top, left-middle, and left-bottom TLs, respectively, and they corresponded to 240, 184, and 248 pixels. The largest errors occurred because of the interference between the targeted TL and adjacent lines, and this interference diminished within 1 s because of the control strategies used in the sixth phase of the proposed automatic line-tracking method. These results indicate that the gimbal was accurately controlled by the proposed line-tracking method. The RMSEs of the other sites showed a similar order, and they are not presented in this article for the sake of brevity.

B. CONSISTENCY DETECTION

Figs. 8 and 9 show the image- and signal-processing procedures in the consistency estimation method (B in Fig. 2), in which each phase was successfully executed. The recorded combined images were converted into the chroma metric form, and stripes were removed in the first phase by using Eqs. (5), (6), and (7) (① in Fig. 8). The preprocessed images were reduced to noise-suppressed 1D images by applying the 3σ outlier method according to Eqs. (8) and (9) in the second phase (② in Fig. 8). The elements of the 1D matrices indicating the PD intensities were mapped to the global coordinate system by using the GPS information recorded in the third phase with Eqs. (10) and (11) (③ in Fig. 8). Finally, the consistency was evaluated from the mapped PD intensities by using the method proposed in Fig. 5 (Figs. 9(a), (c), and (e)), and alarms were generated based on the 2D consistency map (Figs. 9(b), (d), and (f)). The horizontal axis in Fig. 9 represents the relative parallel displacement of the UAV according to the inspection start. Time stamps of the recorded images were combined with GPS information from the flight controller to calculate the relative parallel displacement when the images were recorded. The vertical axes in Figs. 9(a), (c), and (e) denote the consistencies estimated at the relative locations of TLs from the start and those in Figs. 9(b), (d), and (f) denote the relative distances

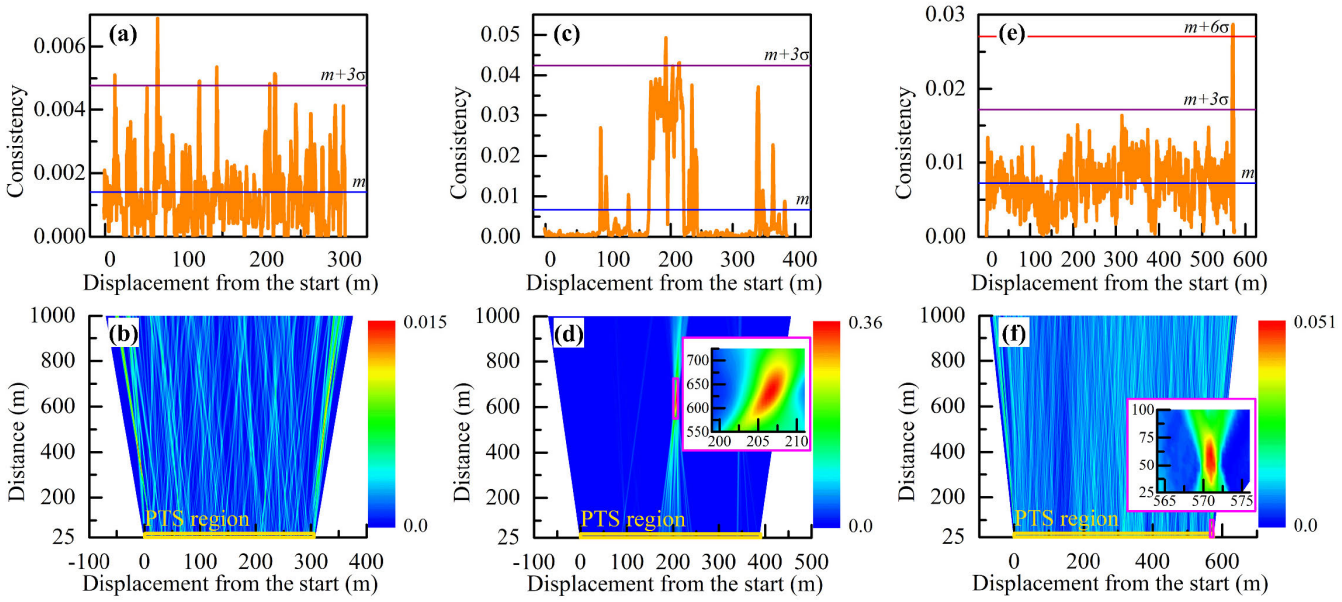

FIGURE 9. Field test results obtained using the consistency estimation method: (a) and (b) Results of the right-bottom line of SB TL 70-71, (c) and (d) results of the left-top line of SB TL 94-95, and (e) and (f) results of the left-middle line of SS TL 40-41.

from the UAV perpendicular to the TL direction. The colors in Figs. 9(b), (d), and (f) denote the consistencies estimated at each location along both axes. A color closer to red means a higher estimated consistency; therefore, the regions with colors close to red correspond to the locations of consistent PD.

The inspection results for SB TL 70-71 show no noticeable PD from the TLs and auxiliary power systems (Figs. 9(a) and (b)). The mean PD during the inspections was exceedingly small compared to those at the other sites because the farmland area had no source of PD. This low mean led to the generation of pre-alarms at several locations (Fig. 9(a)). However, the 2D consistency map shows no high consistency values in the PTS regions (i.e., 25–42.2 m, yellow box in Figs. 9(b), (d), and (f)) compared to those measured at the other sites. Therefore, no final caution alarm was generated for any location of SB TL 70-71.

Figs. 9(c) and (d) shows the inspection results for SB TL 94-95. The mean PD during the inspection was 0.0059, which is almost four times the value for SB TL 70-71 (0.0015), because the TLs pass through an industrial area. Many factories in this district are heavy industries. Hence, PDs at these factories could have been frequent and could have been measured by the SIS because factory operations could have led to strong PD densities. Interestingly, the consistency increased significantly at about 200 m from the start and exceeded 3σ at 192 m. Hence, the 2D consistency map was generated to identify the high-consistency locations. The 2D consistency map (Fig. 9(d)) exhibited high consistency at around 630 m, which did not coincide with the location of the TLs; hence, no final caution alarm was generated.

The recorded images were analyzed to elucidate the origin of the pre-alarm. An inspection image obtained at 200 m from the start showed constant corona discharges from a

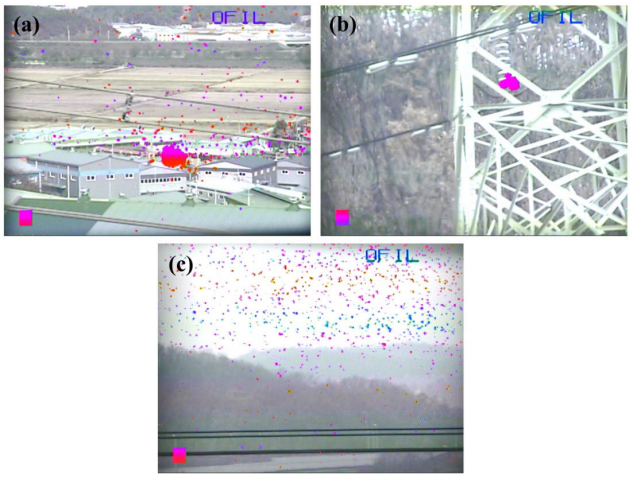

FIGURE 10. Images recorded with the UV camera: (a) An image of the region located around 200 m from the starting tower of SB TL 94-95, (b) image of SS Tl 40-41, and (c) image of SS TL 32-33.

factory (Fig. 10(a)). The factory emitting the PDs was roughly 640 m away from the UAV path and was manufacturing turbines and auxiliary components for power plants. The recorded PDs would have been emitted from welding processes. In conclusion, the proposed method found consistent corona discharge and indicated that it was emitted from the background rather than the TLs.

Figs. 9(e) and (f) shows the inspection results for SS TL 40-41. The order of magnitude of the mean PD recorded during the inspection was similar to that recorded for SB TL 94-95 because several factories surround this district. The estimated consistency was within 3σ, except at the end of the inspection (Fig. 9(e)). Specifically, the estimated consistency was 0.029, which exceeded 6σ at around 580 m from the start, and therefore, a 2D consistency map was generated. In the

consistency map, a consistent PD with a value of 0.05 was found around the transmission tower. Hence, a final warning alarm was generated. Analysis of the inspection image showed that a PD constantly occurred from the ceramic insulators supporting the TLs (Fig. 10(b)).

A precise inspection was conducted: UV images of the suspected insulator were recorded for 1 min, and it was examined whether more than 5000 PDs occurred. However, fewer than 5000 PDs occurred. The expert system analyzed all the data to elucidate the exact origin, and it concluded that this inspection result could be ascribed to two reasons. First, the 345 kV PTS consisted of two-bundle conductors, whereas PTS design guidelines suggest that a 345 kV PTS should be designed with four-bundle conductors. Hence, the electric field of the 345 kV PTS was originally unstable and, therefore, frequently emitted PDs. Second, the inspection was conducted after rains. A high level of moisture and droplets on the winding surface of the insulator resulted in frequent PDs [26]. Thus, the expert system validated the proposed method.

Similarly, SS TL 32-33 was inspected after rains, and many nimbus clouds were present in the sky during the inspection. No PD exceeding 3σ occurred during the inspection. Hence, there were no apparent faults in the TL and auxiliary systems of TL 32-33. However, many PDs occurred in the background, and they originated from the nimbi (Fig. 10(c)). This suggested that the PDs emitted from the nimbus could be measured by the UV camera because of their high density [26], [27]. Hence, we recommend that inspections should be conducted in clear weather conditions. Moreover, this measurement showed that the PD intensity is more important than the distance between the UV camera and the object emitting PDs.

Compared to other methods that can be applied to estimate the PD consistency, such as the simple moving average window method, the proposed method can distinguish consistent PDs from background noise owing to the noise suppression step in the second phase (Eq. (8)). For example, when intense background noise is measured in a subsection of the inspection range, as in Fig. 10(c), the estimated consistency can be high when other methods are applied because intense PDs are constantly observed in the subsection, although they do not originate from the inspection object. However, in the proposed method, evenly distributed noise is suppressed, regardless of its intensity by using Eq. (8) in the second phase. Moreover, concentrated PDs are weighted over background noise when they coexist, as shown in Fig. 10(a). In addition, insufficiently intense PDs are filtered because the PDs with intensities lower than a threshold do not contribute to consistency in the fourth phase, whereas those PDs affect consistency in the other methods. Therefore, with the proposed method, the consistency of PDs from a damaged surface is visualized more distinctly.

V. CONCLUSION

This study presents an SIS based on an embedded nondestructive fault diagnostic method. The SIS was mounted on a UAV and involved not only an automatic line-tracking method for conducting reliable inspections but also a consistency diagnostic method that detected consistent corona discharges effectively, particularly during patrol inspection. Both methods employ several image- and signal-processing methods. The proposed method generates a caution or warning alarm by using a combination of a statistical outlier detection method and an estimated 2D consistency map. Field tests were conducted on 345 kV PTSs. The results showed that the proposed method could detect consistent PDs. Moreover, consistency detection at different target distances can help identify the location of corona discharges and, consequently, distinguish PDs due to defects in PTSs from background PDs. Hence, fault diagnoses can be performed efficiently and conveniently for difficult-to-reach PTSs. Future studies should further validate the method at various sites and develop techniques for the automatic selection of target TLs for patrol inspections.

REFERENCES

[1] G. Andersson, P. Donalek, R. Farmer, N. Hatziargyriou, I. Kamwa, P. Kundur, N. Martins, J. Paserba, P. Pourbeik, J. Sanchez-Gasca, R. Schulz, A. Stankovic, C. Taylor, and V. Vittal, "Causes of the 2003 major grid blackouts in North America and Europe, and recommended means to improve system dynamic performance," *IEEE Trans. Power Syst.*, vol. 20, no. 4, pp. 1922–1928, Nov. 2005.

[2] P. Pourbeik, P. S. Kundur, and C. W. Taylor, "The anatomy of a power grid blackout–root causes and dynamics of recent major blackouts," *IEEE Power Energy Mag.*, vol. 4, no. 5, pp. 22–29, Sep. 2006.

[3] R. Ferraro, *Field Guide: Inspection of Conductors for Overhead Transmission Lines*. Washington, DC, USA: Electric Power Research Institute, 2015.

[4] S. Madakam, R. Ramaswamy, and S. Tripathi, "Internet of Things (IoT): A literature review," *J. Comput. Commun.*, vol. 3, no. 5, pp. 164–173, May 2015.

[5] J. Sawada, K. Kusumoto, Y. Maikawa, T. Munakata, and Y. Ishikawa, "A mobile robot for inspection of power transmission lines," *IEEE Trans. Power Del.*, vol. 6, no. 1, pp. 309–315, Jan. 1991.

[6] J.-Y. Park, J.-K. Lee, B.-H. Cho, and K.-Y. Oh, "An inspection robot for live-line suspension insulator strings in 345-kV power lines," *IEEE Trans. Power Del.*, vol. 27, no. 2, pp. 632–639, Apr. 2012.

[7] H.-S. Park, B. H. Choi, J. J. Kim, and T.-H. Lee, "Seismic performance evaluation of high voltage transmission towers in South Korea," *KSCE J. Civil Eng.*, vol. 20, no. 6, pp. 2499–2505, Nov. 2015.

[8] E. Pastor, J. Lopez, and P. Royo, "UAV payload and mission control hardware/software architecture," *IEEE Aerosp. Electron. Syst. Mag.*, vol. 22, no. 6, pp. 3–8, Jun. 2007.

[9] H. Ha, S. Han, and J. Lee, "Fault detection on transmission lines using a microphone array and an infrared thermal imaging camera," *IEEE Trans. Instrum. Meas.*, vol. 61, no. 1, pp. 267–275, Jan. 2012.

[10] L. Wu, W. He, J. Hu, F. Zhou, B. Song, X. Shen, and T. Xu, "Study on daytime camera for corona discharge detection," *Semicond. Optoelectron.*, vol. 31, pp. 443–446 and 450, Jun. 2010.

[11] G. C. Stone, "Partial discharge diagnostics and electrical equipment insulation condition assessment," *IEEE Trans. Dielectr. Electr. Insul.*, vol. 12, no. 5, pp. 891–904, Oct. 2005.

[12] L. Wang and A. Cavallaro, "Acoustic sensing from a multi-rotor drone," *IEEE Sensors J.*, vol. 18, no. 11, pp. 4570–4582, Jun. 2018.

[13] M. Voller and K. Mollmann, *Infrared Thermal Imaging Fundamentals, Research and Applications*. Hoboken, NJ, USA: Wiley, 2014.

[14] M.-I. Choi and J.-C. Kim, "A study on the signal analysis of corona discharge on the polymer insulator using UV sensor array," *J. Korean Inst. Illum. Electr. Installation Eng.*, vol. 28, no. 4, pp. 16–20, Apr. 2014.

[15] *Standard for Overhead Power Transmission Lines O&M, H0-Power Transmission-Standard-0002*, Korea Electr. Power Corp., Naju-si, South Korea, 2017.

[16] J. Park, S. Kim, J. Lee, J. Ham, and K. Oh, "Method of operating a GIS-based autopilot drone to inspect ultrahigh voltage power lines and its field tests," *J. Field Robot.*, vol. 37, no. 3, pp. 345–361, Apr. 2020, doi: 10.1002/rob.21916.
[17] J. Canny, "A computational approach to edge detection," *IEEE Trans. Pattern Anal. Mach. Intell.*, vol. PAMI-8, no. 6, pp. 679–698, Nov. 1986.
[18] H. Guan, Y. Yu, J. Li, Z. Ji, and Q. Zhang, "Extraction of power-transmission lines from vehicle-borne lidar data," *Int. J. Remote Sens.*, vol. 37, no. 1, pp. 229–247, Jan. 2016.
[19] P. V. C. Hough, "Method and means for recognizing complex patterns," U.S. Patent 3 069 654, Dec. 18, 1962.
[20] V. K. Mehta and R. Mehta, *Principles of Power System*. New Delhi, India: S. Chand, 2004.
[21] R. E. Kalman, "A new approach to linear filtering and prediction problems," *J. Basic Eng.*, vol. 82, no. 1, pp. 35–45, Mar. 1960.
[22] H. D. Cheng, X. H. Jiang, Y. Sun, and J. Wang, "Color image segmentation: Advances and prospects," *Pattern Recognit.*, vol. 34, no. 12, pp. 2259–2281, Dec. 2001.
[23] R. S. Figliola and D. E. Beasley, *Theory and Design for Mechanical Measurements*, 6th ed. Hoboken, NJ, USA: Wiley, 2016.
[24] F. Pukelsheim, "The three sigma rule," *Amer. Statistician*, vol. 48, no. 2, pp. 88–91, May 1994.
[25] T. Vincenty, "Direct and inverse solutions of geodesics on the ellipsoid with application of nested equations," *Surv. Rev.*, vol. 23, no. 176, pp. 88–93, Apr. 1975.
[26] A. A. Sin'kevich and Y. A. Dovgalyuk, "Corona discharge in clouds," *Radiophys. Quantum Electron.*, vol. 56, nos. 11–12, pp. 818–828, Apr. 2014.
[27] B. R. Maskell, "The effect of humidity on a corona discharge in air," Roy. Aircr. Establishment, Farnborough, U.K., Tech. Rep. AD0720090, Jun. 1970.

SAN KIM received the B.S. degree in energy system engineering from Chung-Ang University, Seoul, South Korea, in 2019, where he is currently pursuing the M.S. degree in energy system engineering. His research interests include smart mobility and artificial intelligence for prognostics and health management.

DONGGEUN KIM received the B.S. degree in energy system engineering from Chung-Ang University, Seoul, South Korea, in 2019, where he is currently pursuing the M.S. degree in energy system engineering. His research interests include diagnostic robots for extreme environments, artificial intelligence for diagnostics and prognostics, and design optimization.

SIHEON JEONG received the B.S. degree in energy system engineering from Chung-Ang University, Seoul, South Korea, in 2019, where he is currently pursuing the Ph.D. degree in energy system engineering. His research interests include diagnostics and prognostics with smart mobility, artificial intelligent, simultaneous localization and mapping, and object cognition with novel sensors for autonomous driving and flight of smart mobility.

JI-WAN HAM received the B.S. degree in mechatronics engineering from Chungnam National University, Daejeon, South Korea, in 2010. He is currently pursuing the M.S. degree in energy system engineering with Chung-Ang University. His research interests include artificial intelligence for prognostics and health management, simultaneous localization and mapping, and object cognition for autonomous driving and flight for smart mobility.

JAE-KYUNG LEE received the B.S. degree in electrical engineering from Kyungpook National University, Daegu, South Korea, in 2002, and the M.S. degree in electrical engineering from KAIST in 2004. He is currently a Senior Researcher with the Power Transmission Laboratory, KEPCO Research Institute. His research interests include the development of high-performance robot control, hazardous robot systems, and SCADA/condition monitoring systems for wind turbines.

KI-YONG OH received the B.S. degree from Hanyang University, Seoul, South Korea, in 2005, the M.S. degree from KAIST in 2006, and the Ph.D. degree from the University of Michigan, Ann Arbor, MI, USA, in 2016, all in mechanical engineering.

He joined the School of Energy System Engineering, Chung-Ang University, in 2017, where he is currently employed as an Assistant Professor. His teaching and research interests include applied dynamics, and prognostics and health management in the field of complex energy systems.